CHEMISTRY OF MATERIALS
Article

Chem. Mater. **2009,** *21,* 2641–2649 2641
DOI:10.1021/cm803379n

Proton Dynamics in In:$BaZrO_3$: Insights on the Atomic and Electronic Structure from X-ray Absorption Spectroscopy

Francesco Giannici,*[,†] Alessandro Longo,[‡] Antonella Balerna,[§] Klaus-Dieter Kreuer,[⊥] and Antonino Martorana[†,‡]

[†]*Dipartimento di Chimica Inorganica e Analitica "Stanislao Cannizzaro", Università di Palermo, Viale delle Scienze, I-90128 Palermo, Italy,* [‡]*Istituto per lo Studio dei Materiali Nanostrutturati, Consiglio Nazionale delle Ricerche, Via Ugo La Malfa 153, I-90146 Palermo, Italy,* [§]*Laboratori Nazionali di Frascati, Istituto Nazionale di Fisica Nucleare, Via Enrico Fermi 44, I-00044, Frascati, Italy, and* [⊥]*Max-Planck-Institut für Festkörperforschung, Heisenbergstrasse 1, D-70569 Stuttgart, Germany*

Received December 15, 2008. Revised Manuscript Received April 29, 2009

The local structure of Ba^{2+}, Zr^{4+}, and In^{3+} in In:$BaZrO_3$ is investigated with EXAFS for samples having 0 to 75% In^{3+} content. It is found that indium can be inserted in any ratio in the host matrix oxide and that the oxygen coordination shell displays an in−O distance very similar to the Zr−O length. In the Zr-rich compositions, there is a preferred dopant-vacancy association that, however, does not give rise to dopant-proton interaction in the hydrated samples. The tendency of Ba^{2+} to be attracted toward the dopant site is attributed to the electrostatic interaction with the dopant and to the structural rearrangement around the In^{3+} site. Third cumulant analysis at high temperatures (up to 673 K) allows to conclude that the anharmonicity of In−O thermal motion is about 1 order of magnitude lower than in other perovskites with higher proton conductivity. It is argued that the lower proton diffusivity displayed by In:$BaZrO_3$ depends on (a) proton trapping at the dopant site due to the formation of a stable O−H···O hydrogen bond; (b) reduced anharmonicity of the M−O vibrations; (c) different strength of O−H bonds originated by electronic density rearrangement.

1. Introduction

Doped barium cerate has always been the benchmark for oxide proton conductors, and is the most extensively studied compound. However, its poor stability with respect to carbonate formation has diverted interest in the more symmetric barium zirconate, most notably in yttrium-doped barium zirconate: this has, however, proven to suffer from a dopant-rich phase segregation in grain boundaries, for which to date no effective solutions have been found.[1] In earlier work, we have addressed the conductivity and phase stability issues in Y-doped, Gd-doped, and In-doped barium cerate from the EXAFS local structure point of view.[2−5] In this latter work, we reported that single-phase solid solutions $BaCe_{1-x}In_xO_{3-\delta}$ can be synthesized in the $0.02 < x < 0.75$ range, and that they show interesting proton conductivity (0.001 S cm^{-1} at 673 K in wet N_2 for $BaCe_{0.7}In_{0.3}O_{3-\delta}$). In the present paper, we present a thorough account of the local structure around each cation in hydrated and dry $BaZr_{1-x}In_xO_{3-\delta}$, with $0 < x < 0.75$, at different temperatures. The present local structure analysis, in combination with neutron diffraction literature data, impedance and TGA results, allows us to draw general conclusions about the electronic and geometrical factors coming into play in the doped materials, and their effect on both the global lattice dynamics and the proton conductivity. Throughout the following, doped perovskites will be tagged by three-letter acronyms, such as BZI for indium-doped barium zirconate, BCY for yttrium-doped barium cerate, and so on, followed by a number indicating the Zr-site doping percentage.

The peculiar ability of In^{3+} to enter into barium cerate and zirconate in virtually any amount has obviously driven much interest: although the proton diffusivity values are lower if compared to yttrium-doped barium zirconate, there are some possible advantages when it comes to phase segregation and high proton concentration. These have recently led to the investigation of heavily doped $BaZr_{1-x}In_xO_{3-\delta}$ and related $Ba_2In_2O_5$ structures in a number of detailed neutron scattering, vibrational spectroscopy, and computational papers.[6−14]

*Corresponding author. E-mail: giannici@pa.ismn.cnr.it.

(1) Kreuer, K.-D. *Annu. Rev. Mater. Res.* **2003**, *33*, 333.
(2) Longo, A.; Giannici, F.; Balerna, A.; Ingrao, C.; Deganello, F.; Martorana, A. *Chem. Mater.* **2006**, *18*, 5782.
(3) Giannici, F.; Longo, A.; Deganello, F.; Balerna, A.; Arico, A. S.; Martorana, A. *Solid State Ionics* **2007**, *178*, 587.
(4) Giannici, F.; Longo, A.; Balerna, A.; Martorana, A. *Chem. Mater.* **2009**, *21*, 597.
(5) Giannici, F.; Longo, A.; Balerna, A.; Kreuer, K.-D.; Martorana, A. *Chem. Mater.* **2007**, *19*, 5717.
(6) Berastegui, P.; Hull, S.; García-García, F. J.; Eriksson, S.-G. *J. Solid State Chem.* **2002**, *164*, 119.
(7) Ahmed, I.; Eriksson, S.-G.; Ahlberg, E.; Knee, C. S.; Berastegui, P.; Johansson, L.-G.; Rundlöf, H.; Karlsson, M.; Matic, A.; Börkesson, L.; Engberg, D. *Solid State Ionics* **2006**, *177*, 1395.
(8) Karlsson, M.; Björketun, M. E.; Sundell, P. G.; Matic, A.; Wahnström, G.; Engberg, D.; Ahmed, I.; Eriksson, S.; Berastegui, P. *Phys. Rev. B* **2005**, *72*, 094303.
(9) Karlsson, M.; Matic, A.; Knee, C. S.; Ahmed, I.; Eriksson, S. G.; Börjesson, L. *Chem. Mater.* **2008**, *20*, 3480.

Published on Web 05/18/2009

In particular, neutron diffraction data shows a quite unusual sigmoidal increase in the unit-cell volume as a funcion of In^{3+} fraction, for which no explanation has to date been proposed.[7] Karlsson et al. argued on the basis of Raman data analysis that the parent cubic arrangement of $BaZrO_3$ is modified by the guest In^{3+} cation, resulting in a tilting of the $(In/Zr)O_6$ octahedra.[9] DFT calculations with different trivalent dopants in $BaZrO_3$ showed that a larger electronic charge on oxygen atoms does not affect the strength of O−H bonds, and the height of the migration barriers.[14]

Despite the considerable amount of work on proton-conducting zirconates, there are almost no accounts about the local structure and its correlation with lattice dynamics. Actually, apart from a partial investigation about site selectivity in $CaZrO_3$ reported several years ago,[15] the results discussed herein on BZI constitute the first systematic EXAFS report of local structure in these materials, accounting also for the discrimination between static and vibrational disorder and for the analysis of lattice anharmonicity. The discussion is centered on the local structure around Zr^{4+} and In^{3+}, with Supporting Information about the average structure coming from the Ba^{2+} environment. To derive a comprehensive picture of the influence of dopant in BZI, the structural results are correlated with informations about the proton incorporation and dynamics, coming from thermogravimetry and impedance and vibrational spectroscopy.

2. Experimental Section

2.1. Synthesis and Laboratory Characterization. Barium carbonate (>99%, Fluka), zirconium oxide (TZ-0, Tosoh), and indium oxide (99.9%, Alfa Aesar) were used as starting compounds. The powders were mixed in ethanol and calcined at 1373 K for 2 h, then ball milled for 1 h, calcined at 1573 K overnight, and planetary milled for 2 h. A portion of the powders was dried in pure N_2 at 973 K for 6 h to completely remove water, yielding samples labeled as DRY. Another portion was equilibrated in wet N_2 at 573 K overnight to achieve maximum proton content. The XRD patterns were recorded with a PW1050 diffractometer (Philips) equipped with a graphite monochromator, using Cu Kα radiation in Bragg−Brentano geometry from 10 to 90° 2θ. The diffraction profiles were modeled with GSAS, using a cubic $Pm\bar{3}m$ unit cell.[16] Pellet preparation and details of the impedance spectroscopy (IS) measurements are described in a previous paper.[5] IS was performed in either wet (P_{H_2O} = 23 hPa) or dry N_2 to separate protonic and oxygen vacancy contributions to conductivity, with electron and electron hole concentration being far too low to be signifcant. Thermogravimetric traces of water incorporation were recorded on the powders using a thermostatted Sartorius 7014 balance in wet N_2, and the curves were fitted as described previously to extract the thermochemical parameters of the hydration reaction.[5]

2.2. X-ray Absorption. X-ray absorption spectra were recorded at the GILDA BM8 and BM29 beamlines of the European Synchrotron Radiation Facility (ESRF) using a double-crystal monochromator equipped with Si(311) crystals for Zr K-edge (18 keV) and In K-edge (28 keV), and with Si(511) crystals for Ba K-edge (37 keV). For In K-edge on BZI2, fluorescence spectra were taken with a 13-elements detector and the monochromator was operated in dynamical focusing mode to maximize the flux. High-temperature measurements were taken using an in situ thermochemical cell.[17] All data were extracted with a Bayesian algorithm and fitted using the program Viper.[18] Theoretical amplitudes and phases were calculated with FEFF8.4: scattering paths involving In and Zr were weighed appropriately to account for random mixing on the Zr-site.[19] During analysis and in all the figures, the EXAFS data are weighted by k^2. Unless otherwise noted, the figures and tables always refer to the low-temperature spectra (25 K).

3. Results and Discussion

A BZI fragment cut from the cubic $Pm\bar{3}m$ crystal structure is drawn in Figure 1 to allow the recognition of photoelectron paths used for Zr and In K-edge EXAFS analysis. Eight interconnected MO_6 (M = Zr, In) octahedra and the barium atom embedded in the central cavity are included in the figure. The photoabsorber atom (on the left) is labeled as Zr(In); the oxygen first and second neighbors of Zr(In) are called O1 and, respectively, O2; similarly, M1 and M2 are the B-site neighbors.

3.1. EXAFS on the Zr K-Edge. The results from the analysis of BZ and BZI on the Zr K-edge are reported in Table 1. With reference to the scheme of Figure 1, single Zr−O and Zr−Ba distances were used and the Zr−M1 and Zr−O1−M1 interoctahedral distances were constrained to be equal, with no tilt between neighboring octahedra. The next-neighboring octahedra were modeled with a single Zr−M2 interoctahedral distance. In addition to the paths belonging to the first three shells Zr−O1, Zr−Ba, Zr−M1, the following paths were used: (a) the fourth-shell single-scattering Zr−O2; (b) the related Zr−O2−O1 multiple scattering (MS) path (with geometrically constrained path length); (c) the intraoctahedral Zr−O1−Zr−O1 linear configuration, involving first neighbors O1 oxygens lying at opposite octahedral vertices, with overall path length $R = 2R_{O1}$. To keep the number of free parameters to a minimum, we used a single Debye−Waller factor (σ^2_{O1}) for all paths involving oxygen atoms, assuming that the anion disorder is large if compared to the cation sublattice, and uncorrelated to it. Examples of the data and fitting quality are plotted in Figures 2 and 3.

(10) Stølen, S.; Mohn, C. E.; Ravindran, P.; Allan, N. L. *J. Phys. Chem. B* **2005**, *109*, 12362.
(11) Stølen, S.; Bakken, E.; Mohn, C. E.; Matter, S. *Phys. Chem. Chem. Phys.* **2006**, *8*, 429.
(12) Islam, M. S.; Davies, R. A.; Fisher, C. A. J.; Chadwick, A. V. *Solid State Ionics* **2001**, *145*, 333.
(13) Martinez, M.; Mohn, C. E.; Stølen, S.; Allan, N. L. *J. Solid State Chem.* **2007**, *180*, 3388.
(14) Björketun, M. E.; Sundell, P. G.; Wahnström, G. *Phys. Rev. B* **2007**, *76*, 054307.
(15) Davies, R. A.; Islam, M. S.; Chadwick, A. V.; Rush, G. E. *Solid State Ionics* **2000**, *130*, 115.
(16) Larson, A.; Von Dreele, R. B. *Report LAUR* **1988**, 86.
(17) Longo, A.; Balerna, A.; D'Acapito, F.; D'Anca, F.; Giannici, F.; Liotta, L. F.; Pantaleo, G.; Martorana, A. *J. Synchrotron Rad.* **2005**, *12*, 499–505.
(18) Klementev, K. D. *J. Phys. D: Appl. Phys.* **2001**, *34*, 209.
(19) Ankudinov, A. L.; Ravel, B.; Rehr, J. J.; Conradson, S. D. *Phys. Rev. B* **1998**, *58*, 7565.

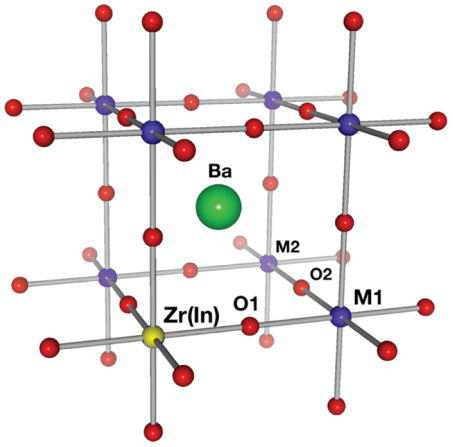

Figure 1. Scheme of the lattice fragment used for the EXAFS model.

Table 1. Structural Parameters of Zr^{4+} Local Environment in BZI Derived from EXAFS Analysis[a]

	Zr−O1		Zr−Ba		Zr−M1		Zr−O2	Zr−M2	
	R	σ^2	*R*	σ^2	*R*	σ^2	*R*	*R*	σ^2
BZ	2.10	3.0	3.63	2.4	4.20	1.4	4.67	5.90	2.7
BZI2	2.11	3.9	3.63	2.8	4.20	2.9	4.67	5.95	2.7
BZI2DRY	2.11	3.9	3.63	2.8	4.20	2.9	4.67	5.95	2.7
BZI10	2.11	4.4	3.64	2.8	4.21	2.7	4.66	5.95	2.7
BZI10DRY	2.10	4.1	3.63	2.7	4.20	2.6	4.66	5.94	2.4
BZI15	2.10	4.2	3.64	2.9	4.20	2.8	4.66	5.95	2.8
BZI15DRY	2.10	3.7	3.63	2.6	4.21	2.5	4.66	5.95	2.5
BZI20	2.10	3.9	3.64	3.1	4.21	2.9	4.66	5.95	3.2
BZI20DRY	2.10	4.1	3.63	2.9	4.21	2.9	4.66	5.95	2.8
BZI50	2.10	3.8	3.64	4.2	4.19	3.4	4.66		
BZI50DRY	2.10	3.6	3.63	3.8	4.19	3.2	4.66		
BZI75	2.10	4.1	3.62	5.5	4.18	4.8	4.66		
BZI75DRY	2.10	3.7	3.62	4.8	4.18	2.7	4.66		

[a] Distances are in Å, Debye−Waller factors are $\times 10^{-3}$ Å^2. Uncertainty is on the last digit.

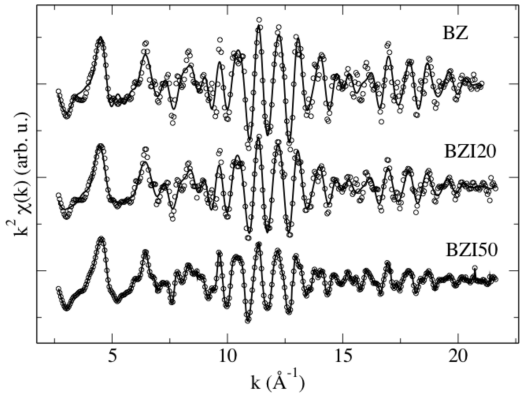

Figure 2. EXAFS spectra (circles) and best fits (line) at the Zr K-edge for BZ, BZI20, and BZI50.

The first-shell Zr−O1 coordination is remarkably unchanged throughout the whole series from BZ to BZI75. First, this applies to the coordination number, so that even for BZI75DRY Zr^{4+} is in octahedral coordination within the sensitivity of the EXAFS analysis. The deviation of N_{O1} from 6 was not significant for any of the samples, and therefore it was kept fixed in the final refinements. As a graphical example, Figure 4 reports the BZI10 and BZI75DRY FT spectra: the first-shell

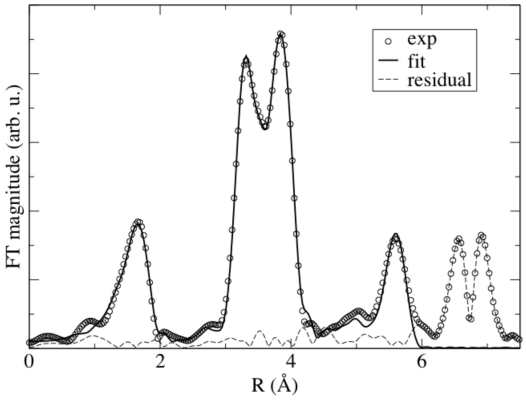

Figure 3. FT EXAFS data (circles), best fit (thick line), and residual (dashes) at the Zr K-edge for BZ.

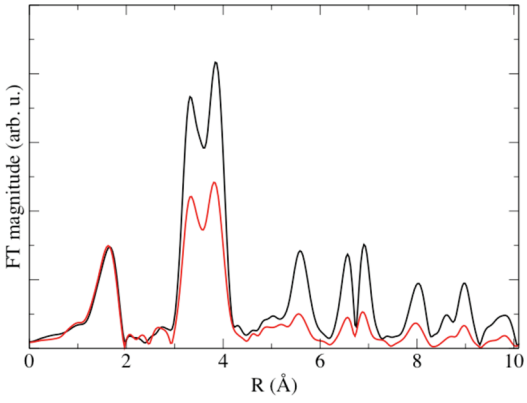

Figure 4. FT EXAFS data on the Zr K-edge for BZI10 (black line) and BZI75 (red line). The first peak around 1.7 Å corresponds to the Zr−O1 first shell. The second and third peaks between 3 and 4 Å come from Zr−Ba and Zr−M1 second and third shells, respectively.

Zr−O1 peaks fall remarkably well on top of one another, whereas the other peaks are distinctly lowered as a result of the higher disorder factors. Nonetheless, the existence of less-coordinated Zr atoms is worth being considered in more detail, especially for the possible tetrahedral coordination resembling the $Ba_2In_2O_5$ brownmillerite-type structure, in which In^{3+} occupies alternatively tetrahedral and octahedral sites.[6] More light on the geometry of the Zr^{4+} environment in highly defective states can be shed using also XANES spectroscopy. The differences in the near-edge features between undoped BZ and BZI75-DRY involve almost only the multiple scattering resonances, that are damped in the latter; however, the overall shape of the edge is unchanged, suggesting that the Zr^{4+} sites remain in an octahedral environment (Figure 5a). The XANES spectra simulated using the full multiple scattering (FMS) capabilities of the FEFF code confirm this observation: the simulated spectrum of undoped BZ, using self-consistent potentials and FMS up to 6.5 Å, reproduces all the features of the experimental edges with good accuracy also in the energy positions. On the other hand, the simulation of Zr^{4+} in a brownmillerite-like tetrahedral site confirms that the presence of ZrO_4 tetrahedra would involve dramatic effects on the shape of the whole XANES spectrum (Figure 5b). Zr^{4+} tetrahedral coordination is therefore definitely excluded.

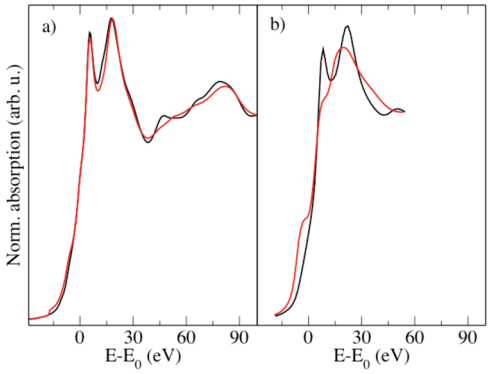

Figure 5. XANES on the Zr K-edge: (a) Experimental spectra for BZ (black line) and for BZI75DRY (red line). (b) Theoretical simulations of Zr^{4+} in an octahedral environment (black line) and in a tetrahedral environment (red line).

The Zr−O1 bond length is almost unchanged in the whole series, at around 2.10 Å. In a previous study of Zr-doped $BaTiO_3$, Laulhè and co-workers reported that the ZrO_6 octahedra are tremendously rigid, so that the internal strains due to the cation substitution lead to a number of effects, e.g., limited overall solubility, and segregation of Zr-rich nanoregions.[20] The present results support the idea of rigid ZrO_6 units.

The Zr−O1 disorder factors in BZI undergo a steplike increase from BZ (0.0030(5) Å^2) to BZI2 (0.0039(5) Å^2), then remaining almost constant around 0.004 Å^2 throughout the rest of the series. A steplike behavior in the Debye−Waller factor can be recognized also for the Zr-M1 correlation, involving the interaction of two octahedral cations with the interposed oxygen (Table 1). These evidence indicate that In^{3+} is able to perturb the whole structure even at very low concentration (for BZI2 there is about one dopant every 4 × 4 × 3 supercell), suggesting that a modification of the host oxide electronic band structure takes place.

3.2. EXAFS on the In K-Edge. The results of the EXAFS analysis on In K-edge in BZI are reported in Tables 2 and 3. Examples of the data and fit quality are depicted in Figures 6 and 7. The first coordination shell around In^{3+} was always satisfactorily fitted using a single In−O1 distance: thus, no distortion of the InO_6 octahedra was observed. The intraoctahedral MS path In−O1−In−O1 in BZI is critical to achieve a good agreement with the data. On the contrary, the corresponding paths of the cerate systems BCY, BCI and BCG are affected by ample bending motions and give rise to drastically damped EXAFS signals.

In some cases, the anion defectivity arising from charge compensation after doping is high enough to influence the coordination number of the first shell. Actually, an F-test applied to the first shell analysis demonstrated that refining the In−O coordination number significantly improved the fit quality for all the dry samples and also for BZI75. Therefore, an additional free N_{O1} parameter was introduced in the models for these samples, with

(20) Laulhé, C.; Hippert, F.; Kreisel, J.; Maglione, M.; Simon, A.; Hazemann, J. L.; Nassif, V. *Phys. Rev. B* **2006**, *74*, 014106.

Table 2. Structural Parameters of In^{3+} Local Environment in BZI2 and BZI2DRY Derived from EXAFS Analysis[a]

	In−O1			In−Ba		In-M1		In−O2	In-M2	
	N	*R*	σ^2	*R*	σ^2	*R*	σ^2	*R*	*R*	σ^2
BZI2	6	2.14	5.8	3.57	6.2	4.20	4.8	4.53	5.88	6
BZI2DRY	6	2.14	5.4	3.57	6.4	4.20	4.9	4.54	5.88	7

[a] Distances are in Å, Debye−Waller factors are × 10^{-3} Å^2. Uncertainty is on the last digit.

Table 3. Structural Parameters of In^{3+} Local Environment in BZI Derived from EXAFS Analysis[a]

	In−O1			In−Ba1 (× 6)		In−Ba2 (× 2)		⟨In−Ba⟩	In−M1	
	N	*R*	σ^2	*R*	σ^2	*R*	σ^2	*R*	*R*	σ^2
BZI10	6	2.12	6.4	3.59	5.9	3.76	3.5	3.63	4.21	3.5
BZI10DRY	5.4	2.10	7.5	3.59	5.8	3.75	3.5	3.63	4.21	3.2
BZI15	6	2.12	6.2	3.59	6.4	3.75	3.8	3.63	4.20	3.6
BZI15DRY	5.4	2.11	5.2	3.57	5.1	3.74	3.3	3.61	4.21	3.2
BZI20	6	2.12	8.5	3.59	8.1	3.76	4.9	3.63	4.20	4.5
BZI20DRY	5.4	2.11	5.8	3.57	5.1	3.74	3.8	3.61	4.21	3.5
BZI50	6	2.12	6.7	3.58	10	3.73	6.0	3.62	4.23	5.5
BZI50DRY	5.8	2.11	6.3	3.56	8.1	3.73	4.9	3.60	4.22	5.6
BZI75	5.6	2.11	6.4	3.51	10	3.68	6.1	3.55	4.24	7.3
BZI75DRY	5.6	2.10	6.5	3.51	9.1	3.68	5.4	3.55	4.23	6.2

[a] Distances are in Å, Debye−Waller factors are × 10^{-3} Å^2. Uncertainty is on the last digit.

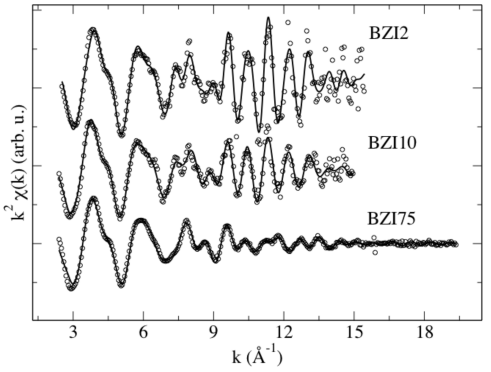

Figure 6. EXAFS spectra (circles) and best fits (line) at the In K-edge for BZI2, BZI10, and BZI75. The higher experimental noise of the BZI2 is due to the fluorescence detection mode, which does not, however, affect the reliability of the analysis.

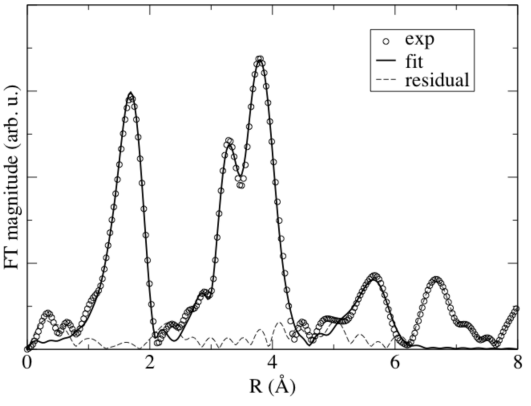

Figure 7. FT EXAFS data (circles), best fit (thick line), and residual (dashes) at the In K-Edge for BZI2.

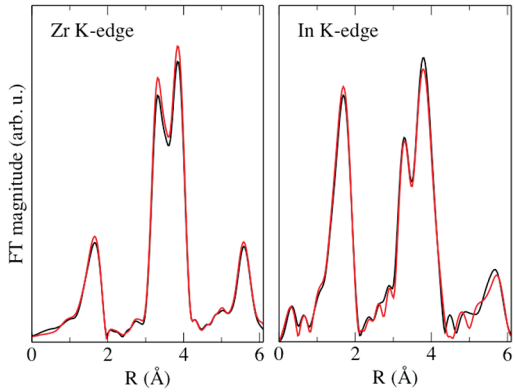

Figure 8. Local structure around Zr^{4+} (left panel) and In^{3+} (right panel) in BZI2 (black line) and BZI2DRY (red line).

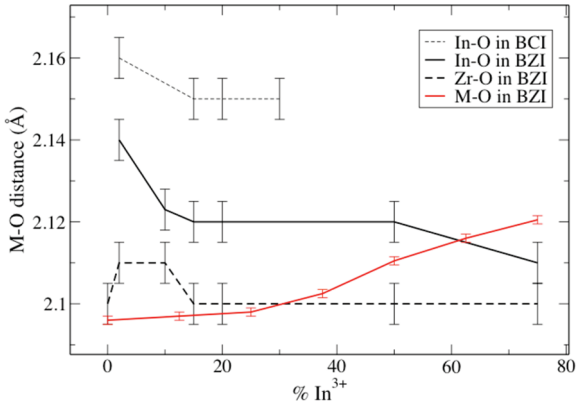

Figure 9. In−O distances in BCI (thin dashes) and BZI (thick line), Zr−O distances in BZI (thick dashes), and the average M−O distance in BZI from neutron diffraction (red line), as a function of the dopant concentration. Data for BCI from ref 5, diffraction data from ref 7.

constrained weighting of all the associated MS paths. At doping level $<50\%$, the N_{O1} coordination number for dry samples is lower than the value corresponding to random vacancy distribution, being therefore indicative of a dopant-vacancy association; on the other hand, at indium concentration $>50\%$ no clear indium-vacancy association takes place.

The In−O disorder variations between the dry and hydrated states suggest some kind of influence of the protons on the local environment of the dopant, although not for all compositions. However, the next-neighboring shells are substantially not affected by protonation, in contrast to what we observed for Y^{3+} dopant in BCY and for Gd^{3+} dopant in BCG.[3,4] In Figure 8, both Zr and In K-edges are plotted for BZI2 and BZI2DRY, showing almost no differences in the In^{3+} environment, and only very slight differences in the Zr^{4+} environment between the two states that, on the other hand, are clearly different in proton concentration, as demonstrated by the discrepancy of 2−3 orders of magnitude in conductivity (the activation energy also changes from 0.4 to 1.1 eV as a result of the change from proton to oxide-ion conduction). Therefore, it can be concluded that the In^{3+} local environment, like in BCI,[5] is not significantly influenced by protonation.

In BCI2 to BCI30, we observed In−O bond lengths between 2.17 and 2.15 Å, slightly decreasing with increasing In^{3+} content.[5] The present results for BZI also show In−O bond length contraction upon increase of dopant concentration, going from 2.14 to 2.10 Å. This tendency is depicted in Figure 9, along with the average M−O distance determined by neutron diffraction. The O−O distances in BZI derived from the present results are in the 3.03−2.97 Å range (3.07−3.04 in BCI). An In^{3+} ionic radius of 0.77−0.70 Å can thus be deduced, exceedingly smaller than the tabulated value. The results hold in the hydrated state too, when the vacancies are all nominally filled, so that the In−O contraction can not be attributed to the lowering of the coordination number. The drawbacks of applying fixed ionic radii to solid solutions were nicely discussed in a seminal EXAFS study on YSZ.[21]

As a matter of fact, it is not even sure that one can speak of a clearly defined ionic radius for In^{3+} even in nondoped materials, because regular InO_6 octahedra are found to adopt a wide range of sizes in compounds such as $MnInO_3$ (In−O 2.20 Å), $CdIn_2O_4$ (2.20 Å), $MnIn_2O_4$ (2.12 Å), $Ba_2InRu_2O_9$ (2.07 Å), $Ba_3InLaW_2O_{12}$ (2.03 Å).[22−26] It is not surprising that in $BaZrO_3$ the In^{3+} dopant can easily adapt to match the host structure. We have previously proposed that this mimicking ability originates from the very low absolute hardness of In^{3+}, involving easy polarizability and therefore the ability of releasing lattice strains produced by size mismatch.[5] The almost complete solubility of indium, both in BZ and BC, is likely a consequence of the electronic properties. With reference to Figure 9, we can divide the behavior of the BZI system in three regions: in the Zr-rich side, the average lattice spacing probed by diffraction changes smoothly, because the InO_6 octahedra can adapt their size to release the "chemical pressure" generated by presence of the smaller and tougher ZrO_6 octahedra. From 20 to 50% indium content, the two cations generally retain a well-defined size, and the lattice parameter grows constantly with composition. Finally, in the In-rich region, the defectivity of the lattice is very high and the complex relation between local and long-range structures will be discussed below.

The cubic model of the local structure around Zr^{4+} was successfully used also to analyze the In K-edge data for both BZI2 and BZI2DRY (Table 2). The In−Ba second shell is very contracted if compared to Zr−Ba, in spite of the larger size of the InO_6 octahedron. A local cubic symmetry is maintained around In^{3+}, confirmed by the high contribution to the total EXAFS signal of the In−O2 cage at about 4.5 Å; the In−Ba length contraction is

(21) Li, P.; Chen, I.-W.; Penner-Hahn, J. E. *Phys. Rev. B* **1993**, *48*, 10074.
(22) Giaquinta, D. M.; zur Loye, H.-C. *J. Am. Chem. Soc.* **1991**, *114*, 10952.
(23) Rasines, I. *Z. Kristallogr. Krist.* **1974**, *140*, 410.
(24) Pokrovskii, B. I.; Gapeev, A. K.; Pokholov, K. V.; Komissarova, L. N.; Igonina, I. V.; Babeshkin, A. M. *Kristallografiya* **1972**, *17*, 793.
(25) Schaller, H. U.; Kemmler-Sack, S. *Z. Anorg. Allg. Chem.* **1981**, *473*, 178.
(26) Rother, H. J.; Kemmler-Sack, S. *Z. Anorg. Allg. Chem.* **1980**, *465*, 179.

then due to only an effective negative charge residing on the doped B-site, rather than to structural rearrangement.

On the other hand, the cubic model is not suited to reproduce the In^{3+} environment for all the other samples, from BZI10 to BZI75. A severe misfit appeared between the second and third FT peaks when a cubic symmetric model was used around In^{3+} for 10% doping and higher. The fit quality critically improved when the second In−Ba shell was split in two contributions, 6-fold and 2-fold, thus resembling the Ce−Ba split symmetry in barium cerate (see Table 3). It is likely that both smaller electrostatic repulsion and structural rearrangement are effective in pulling some of the Ba^{2+} cations toward the dopant site, while others are pushed far away; this configuration could also be consistent with a tilting of InO_6 octahedra in a perovskite framework, as supposed by Karlsson and co-workers.[9] A similar contraction around the dopant was observed in cerate systems (Gd:$BaCeO_3$, In:$BaCeO_3$, and Y:$BaCeO_3$). This effect is remarkably independent of the dopant size and its size misfit with Ce^{4+}. The contraction seems to be related in a complicated way to the modifications of electronic charge distribution induced by the dopant and to the matrix crystal structure.[4]

The almost complete solubility of In in barium zirconate could be accomplished by a structural arrangement resembling, at high indium content, the browmillerite $Ba_2In_2O_5$ ordered sequence of tetrahedral and octahedral sheets. To investigate this aspect, in the two panels of Figure 10, we show the EXAFS theoretical signals around each site separately. The octahedral site (Figure 10a) closely resembles a normal perovskite, with separated contributions for the 8-fold In−Ba correlation at around 3.66 Å, and the 6-fold In−In correlation between 4.20 and 4.26 Å. The tetrahedral sites, on the contrary, show a completely different fingerprint in the FT plot, with a wide range of In−Ba and In−In having distances between 3.45 and 4.20 Å and a distinct peak around 3.5 Å, that represents then the main difference between the brownmillerite and the perovskite local structure. In Figure 11, the BZI50, BZI75, and $Ba_2In_2O_5$ FT EXAFS spectra are shown, in order to better elucidate the In^{3+} environment of indium-rich BZ compounds. The fingerprint of the brownmillerite tetrahedral environment of indium is completely absent, giving strong evidence that In^{3+} intermixes homogeneously with Zr^{4+} and that there is no significant $Ba_2In_2O_5$ segregation, even on the nanometer scale. However, in the BZI50, and even more in the BZI75 FT spectra, there is a progressively increasing resemblance with the octahedral site of a brownmillerite, with the In−Ba peak contracting and the In−M peak expanding with respect to the configuration of the perovskite. This observation would be consistent with a $Ba_2InZrO_{5.5}$ brownmillerite whose octahedral sites are filled by In^{3+}, and tetrahedral sites are filled by Zr^{4+}, but this possibility is completely ruled out by the above discussion on Zr^{4+} environment. Therefore, it can be ultimately concluded that no tetrahedral coordination is formed, either around Zr^{4+} or In^{3+}, and the oxygen

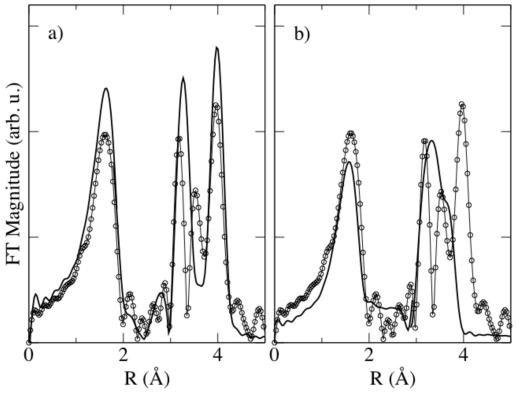

Figure 10. FT EXAFS theoretical signals for $Ba_2In_2O_5$: (a) octahedral site (thick line); (b) tetrahedral site (thick line). Experimental data (circles + thin line) is reported for reference in both panels. As a result of the phase shift, the peaks in the plot are shifted by about −0.5 Å with respect to their physical value.

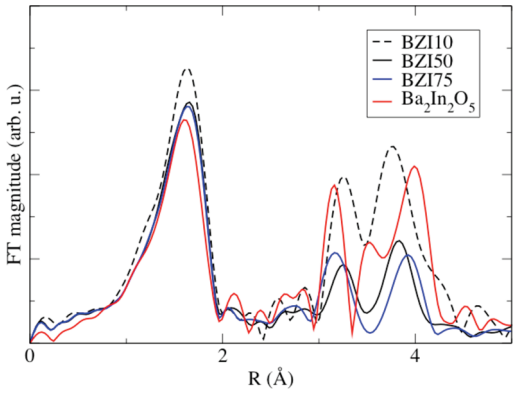

Figure 11. FT EXAFS data on the In K-edge for BZI10 (dashes), BZI50 (black line), BZI75 (blue line), and $Ba_2In_2O_5$ (red line).

vacancies are randomly distributed forming disordered MO_5 polyhedra rather than tetrahedra. This does not give rise to any appreciable change in the diffraction patterns, which have always been indexed as cubic.[7] The high defectivity of the structure induces local rearrangements that resemble more and more the distortions found in the $A_2B_2O_5$ structure, but without any ordering of the vacancies to form MO_4 tetrahedra, or specific long-range effects. This, together with the splitting of the In−Ba distance, provides an explanation for the local distortions detected with Raman spectroscopy.[9]

3.3. EXAFS on the Ba K-Edge. The model used for the Ba K-edge has cubic symmetry, with a 12-fold Ba−O distance, an 8-fold Ba-M distance, and a 6-fold Ba−Ba distance, all with independent Debye−Waller factors. The extreme cases of undoped BZ and BZI50, whose structural parameters are shown in Table 4, are considered to highlight the effects of doping on average structure and dynamics of the lattice. The data and best fittings are shown in the Supporting Information. The Ba−O correlation probes each O^{2-} ion in the samples: the huge disorder increase between BZ and BZI50, always mantaining the cubic symmetry, is due to the presence of both enhanced vibrational movements and significant static disorder coming from the random Zr/In substitution. The fact that the environment around Ba^{2+} remains on

Table 4. Local Structure around Ba^{2+} in BZ, BZI50, and BZI50DRY[a]

	Ba−O			Ba−M		Ba−Ba	
	N	*R*	σ^2	*R*	σ^2	*R*	σ^2
BZ	12	2.98	6	3.61	2.4	4.21	2
BZI50	12	3.02	19	3.62	9.4	4.21	7
BZI50DRY	11	3.02	20	3.62	8.5	4.20	10

[a] Distances are in Å, Debye−Waller factors are $\times 10^{-3}$ Å^2. Uncertainty is on the last digit.

average cubic is consistent with previous results of neutron diffraction.[7] In spite of the three different In−Ba and Zr−Ba distances probed with In and Zr K-edge EXAFS, the Ba−M correlation is seen as one, although quite disordered: its length is totally consistent with the average of all the Zr−Ba and In−Ba distances. However, the quite high disorder factor (on the order of 0.01 Å^2) is indicative of the averaging process over many inequivalent In/Zr sites, and thus it reflects the static disorder. In conclusion, in BZI the Ba^{2+} atoms are 12-fold coordinated with oxygen atoms in a regular or distorted cuboctahedron. Coordination is symmetric for pure BZ, deviating more and more once each Ba^{2+} site is surrounded by doped B-sites. The average Ba−M distance probed by EXAFS therefore arises from the combination of the Zr−Ba and the In−Ba distances shown in Tables 2 and 3. All the Debye−Waller factors increase with In^{3+} concentration, reflecting the static disorder caused by averaging over different Zr−Ba and In−Ba configurations.

3.4. High-Temperature EXAFS. The analysis of the Einstein temperature θ_E provides further evidence about the flexibility of In^{3+} to adapt into host perovskite structures. This parameter is calculated by the following equation[27]

$$\sigma^2_{vib}(T) = \frac{\hbar^2}{2k\mu\theta_E}\coth\left(\frac{\theta_E}{2T}\right)$$

where μ is the reduced mass of the absorber-backscatterer couple and k the Boltzmann constant. Thus, also the static or configurational disorder ($\sigma^2 - \sigma^2_{vib}$), defined as the temperature-independent part of the Debye−Waller factor, can be estimated. The θ_E value for In−O (580 K), is lower than the values for Zr−O and Zr−Ba in barium zirconate (606 K), suggesting the lower stiffness of the lattice around the dopant.

EXAFS analysis at high temperatures also provides some insights on the anharmonicity of the bonds around the absorber: in the case of perovskite proton conductors, it has long been recognized that anharmonic effects in the M−O bonds are beneficial for the proton transfer step.[28] The third cumulant was taken into account for the analysis of the high temperatures EXAFS spectra, according to standard procedure. The results are reported in Table 5 along with structural and disorder parameters. The high quality of experimental data and fitting for

Table 5. Local Structure around In^{3+} in BZI50DRY as a Function of Temperature

	In−O1				⟨In−Ba⟩	In−M1	
T (K)	*N*	*R*	σ^2	C_3	*R*	*R*	σ^2
25	5.8	2.11	6.3	0	3.60	4.22	5.6
80	5.4	2.11	6.8	0	3.60	4.22	5.8
473	5.3	2.11	8.9	0.5	3.61	4.23	13
673	5.3	2.10	12	1.5	3.62	4.24	17
θ_E (K)			600				295
σ^2_{static}			2				5

Distances are in Å, Debye−Waller factors are $\times 10^{-3}$ Å^2, C_3 is $\times 10^{-4}$ Å^3. Uncertainty is on the last digit.

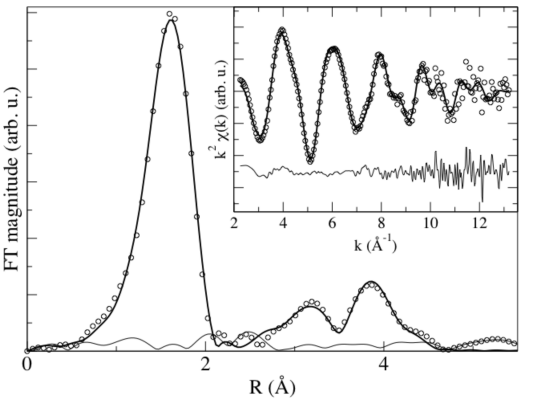

Figure 12. High-temperature EXAFS on the In K-edge: experimental data (circles), best fit (thick line), and residual (thin line) in *R*-space (main plot), and in *k*-space (inset) for BZI50DRY at 673 K.

BZI50DRY at 673 K can be appreciated through inspection of Figure 12. It is worth noticing that at 473 K the third cumulant for In−O correlation in BZI50DRY is 5×10^{-5} Å^3, which is roughly 1 order of magnitude below the corresponding value for BCI15DRY (2×10^{-4} Å^3): the latter is even higher than in BZI50DRY at 673 K. The Y−O and Ce−O third cumulants in BCY10 and BCG10 at 473 K range between 6×10^{-4} and 1×10^{-3} Å^3; therefore, we conclude that the anharmonicity of the In−O bond in BZI50 is small if compared to other doped barium perovskites. Overall, from the analysis of the Debye−Waller factor involving the interactions of indium with its environment in barium zirconate, the picture arises of a rearrangement of the network, likely due to a spread of the In^{3+} excess electronic charge that also influences the interatomic distances.

3.5. Local Structure and Proton Diffusion. TGA shows that the hydration of BZI is almost complete ($[OH^{\bullet}] \approx [In_{Zr}']$) at low temperatures even for the highest In^{3+} concentrations. Figure 13 shows the natural logarithm of the equilibrium constant for the hydration reaction in BZI50 vs inverse temperature, with an evident change in slope around 673 K. BZI75 shows the same qualitative behavior. At higher temperatures, the entropy and enthalpy of hydration are quite low and comparable to the ones reported for BZI10.[29] Below 673 K, both parameters are much more negative, suggesting a higher energetic stabilization of protonic defects and higher degree of

(27) Sevillano, E.; Meuth, H.; Rehr, J. J. *Phys. Rev. B* **1979**, *20*, 4908.
(28) Kreuer, K.-D.; Münch, W.; Ise, M.; Fuchs, A.; Traub, U.; Maier, J. *Ber. Bunsenges. Phys. Chem.* **1997**, *101*, 1344.
(29) Kreuer, K.-D.; Adams, S.; Münch, W.; Fuchs, A.; Klock, U.; Maier, J. *Solid State Ionics* **2001**, *145*, 295.

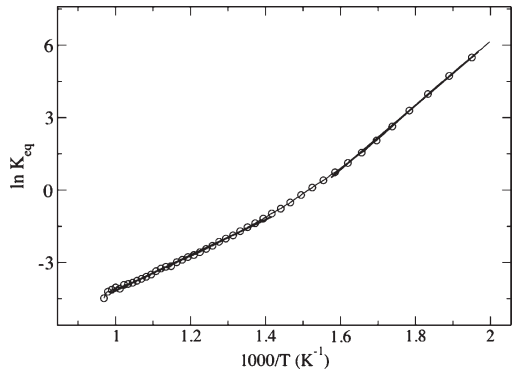

Figure 13. Equilibrium constant for the hydration reaction in BZI50 against inverse temperature. Two linear regimes are evidenced.

order of the protons.[5] The parameters for the high- and low-temperature regions are reported in Table 6.

The results concerning proton diffusion in BZI are reported in Table 7 and Figure 14. Because diffusivity is normalized for charge carrier concentration, this parameter is better suited than conductivity to draw comparisons between different materials, especially at high doping levels. An increasing activation energy can be observed up to 50% indium doping. As discussed in the previous sections, in these materials, only the long-range structure of a cubic perovskite is preserved, whereas at the subnanometer level, the local structure is composed of various configurations that deviate significantly from the cubic symmetry.

The analysis of proton diffusion as a function of dopant concentration was carried out by Kreuer and co-workers for BCY, BCG and BZY.[28−30] The decrease in proton diffusivity of BCY as a function of increasing Y^{3+} content was attributed to a widespread chemical effect of the dopant on the whole lattice, taking into account that the activation energy slowly but steadily increased with the dopant content, whereas the pre-exponential factor was largely unaffected.[31] On the contrary, diffusivity in BZY was enhanced by 1 order of magnitude moving from BZY2 to BZY10. In this case, the activation energy remained constant (0.44 eV), whereas the pre-exponential factor increased dramatically. This effect was ascribed to the high chemical "compatibility" between Zr^{4+} and Y^{3+}, causing a uniform Mulliken population of the oxygen atoms surrounding doped and undoped sites and thus creating a smooth field for proton diffusion.

The overall proton diffusivity in BZI is lower than in BZY and decreases with increasing In^{3+} content: given that the average perovskite framework is maintained, such a decrease may be connected with at least two aspects that emerged in the local structure analysis of BZI: (a) the anharmonicity of lattice vibrations, that was identified as one of the necessary conditions for a good proton conductor and is substantially reduced with respect to other perovskites;[32] (b) the effective relaxation of the zirconate lattice strain originated by In^{3+} size misfit,

(30) Kreuer, K.-D.; Dippel, T.; Baikov, Y. M.; Maier, J. *Solid State Ionics* **1996**, *86−88*, 613.
(31) Kreuer, K.-D. *Solid State Ionics* **1999**, *125*, 285.
(32) Kreuer, K.-D. *Chem. Mater.* **1996**, *8*, 610.

Table 6. Thermochemical Parameters for the Hydration Reaction in BZI as a Dunction of In^{3+} Content

	ΔH^0 (kJ mol^{-1})	ΔS^0 (J mol^{-1} K^{-1})
BZI2	−53	−75
BZI10	−67	−90
BZI50 (> 673 K)	−60	−95
BZI75 (> 673 K)	−74	−109
BZI50 (< 673 K)	−100	−152
BZI75 (< 673 K)	−108	−160

Table 7. Pre-Exponential Factor of Conductivity (S cm^{-1}), Derived Pre-Exponential Factor of Diffusivity ($\times$ 10^{-4} cm^2 s^{-1}), and Activation Energy (eV) for BZI

	σ_0	D_0	E_a
BZI2	0.04	2.2	0.45
BZI10	0.21	2.1	0.48
BZI15	0.375	2.5	0.53
BZI30	0.69	2.3	0.60
BZI50	0.55	1.1	0.62
BZI75	0.67	0.9	0.40

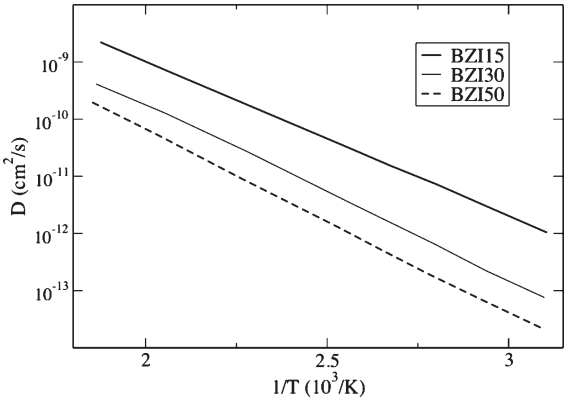

Figure 14. Proton diffusivity vs inverse temperature in a wet N_2 atmosphere for BZI as a function of dopant concentration.

that brings about the complete solubility of the dopant in the matrix. Both aspects seem to be linked with the ability of In^{3+} to rearrange its negative relative charge in the surroundings, thereby modifying the band structure and the O−H bonding states.

Protonation sites in perovskites are typically investigated by neutron diffraction. In the literature, different proton sites have been proposed, allowing for almost free proton reorientation or well established hydrogen bond between neighboring oxygens. Actually, neutron diffraction analyses do not allow us to clearly distinguish between different site symmetries probably because, in doped systems, several proton sites coexist at the same time.[13] The IR study of Karlsson and co-workers, showing the softening of the proton stretching frequency at 2500−3000 cm^{-1} as a function of the dopant amount in BZI, is in agreement with this interpretation and actually the authors propose that the corresponding redshift is originated by the tilting of protons toward charged defects like dopants or vacancies, with the consequent increased tendency to form hydrogen bonds.[8] The low-temperature structure probed by both IR and EXAFS spectroscopies is well in agreement with the TGA results

on BZI, because an effective ordering of O−H bonds in strong hydrogen-bonded configurations, driven also by the local distortion around In^{3+}, results in higher entropy change for the hydration reaction. On the contrary, when the temperature is high enough (> 673 K), the very low entropy of hydration suggests that the special bent configurations are not effective, and protons have enough energy to break the hydrogen bonds.

The influence of dopant local environment on the O−H···O bending is also proposed by Björketun and co-workers in a DFT study mentioned above.[14] These authors find that the electronic charge on the oxygen atoms is uniformly enhanced in hydration conditions, but do not find a corresponding increase in the proton-oxygen interaction energy and migration barriers. They then conclude that the hindrance to proton conduction in BZI should be entirely ascribed to the above outlined trapping effect originated by an enhancement of the hydrogen bond strength. On the other hand, it should also be noted that the plane wave theoretical approach of Björketun and co-workers fails in foreseeing the In−O distance and the activation energy for proton diffusion, whose experimental values, from EXAFS and impedance spectroscopy, are fairly different. As the observed distance and activation energy are to be ascribed to the peculiar electronic properties of In^{3+}, it looks like the influence of the nature of the oxygen-proton bond should be further investigated.

X-ray absorption can only give indirect evidence about protons in the BZI matrix. In particular, the observed attraction of Ba^{2+} toward the negative B^{3+} site can actually support the idea that also other positive charges, and specifically the protons, can be pulled toward the dopant. On the other hand, the nonsensitivity to protonation of the dopant local environment seems to point to a homogeneous distribution of protonation sites so that other factors such as lattice anharmonicity and delocalized electronic rearrangement are also likely affecting proton diffusivity.[37]

(33) Ito, T.; Nagasaki, T.; Iwasaki, K.; Yoshino, M.; Matsui, T.; Igawa, N.; Ishii, Y. *Solid State Ionics* **2007**, *178*, 13.
(34) Ahmed, I.; Knee, C. S.; Karlsson, M.; Eriksson, S.-G.; Henry, P. F.; Matic, A.; Engberg, D.; Börjesson, L. *J. Alloys Comp.* **2008**, *450*, 103.
(35) Knight, K. S. *Solid State Ionics* **2000**, *127*, 43.
(36) Ito, T.; Nagasaki, T.; Iwasaki, K.; Yoshino, M.; Matsui, T.; Igawa, N.; Ishii, Y. *Solid State Ionics* **2006**, *177*, 2353.
(37) Cammarata, A.; Martorana, A.; Duca, D. *J. Phys. Chem. A* **2009**, *00*, 000.

4. Conclusions

Indium can be hosted in the B-site of barium zirconate, like in barium cerate, in any amount. This conclusion of EXAFS spectroscopy validates the results of X-ray and neutron diffraction, excluding the possibility that poorly crystallized indium oxide is present at the highest In concentrations. Although the literature neutron diffraction data do not show any deviation from the cubic symmetry of BZI also for the highest indium content, X-ray absorption, in agreement with Raman spectroscopy, finds evidence of a local distortion around the dopant site. The high solubility of indium in the perovskite BC and BZ networks is to be ascribed to the efficient release of the local strain caused by the ionic radius mismatch with the Zr^{4+} cation of the undoped oxide. This characteristic of In^{3+} involves the ability of the dopant to mimic the doped cation, giving rise to an octahedral oxygen environment definitely smaller than the expected one on the basis of the tabulated ionic radii. The effective negative charge causes a partial collapse of the structure around In^{3+} that could also involve a reduction of the bending of the O−H···O hydrogen bond and in turn a limitation of the freedom of reorientation of the proton among equivalent oxygen neighbors. This conclusion is in agreement with the observed redshift of the proton frequencies of BZI. Other experimental evidence, and in particular the higher harmonicity of the In−O thermal vibration in comparison with that of BCY and BCG and the lower stiffness of In−O, In−Ba, In−M bonds, in comparison with the corresponding Zr bonds, point to an influence of electronic features on the lattice dynamics of In-doped barium zirconate.

Acknowledgment. We thank: Gabi Götz (MPI-FKF) for the XRD measurements; the European Synchrotron Radiation Facility for provision of beamtime, and the staff of beamlines GILDA BM8 and BM29 for support during the EXAFS measurements. Partial financial support from Ministero dell'Università e della Ricerca (PRIN 2006 "Ceramici protonici per celle a combustibile" and FISR "Progetto celle a combustibile") and from Università di Palermo (ex 60%) is acknowledged.

Supporting Information Available: FT plot of EXAFS data and best fit for BZ and BZI50DRY at the Ba K-edge (PDF). k^2-weighted EXAFS raw data at 25K on the Zr K-edge and In K-edge for all samples (PDF). Table of the EXAFS results at 80K on the In K-edge (PDF). This material is available free of charge via the Internet at http://pubs.acs.org.